

# Complex-Valued Stiffness Reconstruction for Magnetic Resonance Elastography by Algebraic Inversion of the Differential Equation

Travis E. Oliphant,<sup>1</sup> Armando Manduca,<sup>2</sup> Richard L. Ehman,<sup>3</sup> and James F. Greenleaf<sup>1\*</sup>

**Noninvasive quantitation of the mechanical properties of tissue could improve early detection of pathology. Previously a method for detecting displacement from propagating shear waves using a phase-contrast MRI technique was developed. In this work it is demonstrated how a collection of data representing the full vector displacement field could be used to potentially estimate the full complex stiffness tensor. An algebraic inversion approach useful for piece-wise homogeneous materials is described in detail for the general isotropic case, which is then specialized to incompressible materials as a model for tissue. Results of the inversion approach are presented for simulated and experimental phantom data that show the technique can be used to obtain shear wave-speed and attenuation in regions where there is sufficient signal-to-noise ratio in the displacement and its second spatial derivatives. The sensitivity to noise is higher in the attenuation estimates than the shear wave-speed estimates. Magn Reson Med 45:299–310, 2001. © 2001 Wiley-Liss, Inc.**

**Key words:** elastography; parameter estimation; phase contrast; shear modulus; tissue characterization

Tissue stiffness can be a more sensitive indicator of pathology than conventionally-imaged parameters such as  $T_1$ ,  $T_2$ , and x-ray density as indicated by the still-routine use of palpation in accessible regions of the body (1). As a result, elastography, which seeks to develop images based on stiffness, has been the subject of significant study (2). Historically, much of this research has been conducted using ultrasound measurements (3–7). With the advent of phase-contrast techniques for measuring static and cyclic displacement using MRI, interest in magnetic resonance elastography (MRE) has been increasing (1,8–11). One reason for the interest in using MR in elastography is that the phase-contrast method used in MRE can provide a full five-dimensional displacement dataset (3D space, 1D time, all polarizations of motion) throughout the region of interest (ROI). While a similar dataset can be obtained with ultrasound interrogation (12), acoustic windows into certain regions of the body are limited, hampering the use of current ultrasonic methods in those regions.

Obtaining stiffness from displacement data requires a reconstruction process that has similarities to inverse scattering methods. Typical inverse scattering problems seek

reconstruction of material parameters using measurements of the scattered field outside of the ROI, coupled with knowledge of the incident field. The reconstruction problem presented by the advent of whole-field displacement measurements seeks determination of the material parameters using measurements of the field inside the ROI. There have been two general approaches to stiffness estimation using such measurements of displacement: static (9) and dynamic (10,11). In the static method, imaging is performed before and after application of a known stress load. The tissue strain estimated from displacement measurements is used to estimate relative tissue stiffness. Estimating absolute tissue stiffness requires knowledge of the material-property boundary conditions using the static technique. Dynamic elastography uses knowledge of displacement collected over time to reconstruct absolute displacement directly. A major advantage of dynamic methods is that absolute estimates of elastic parameters can be obtained with only local knowledge of displacement and its temporal and spatial derivatives.

In this study we test the hypothesis that quantitative estimates of complex-valued stiffness can be obtained from dynamic measurements of internal displacement using direct local inversion of the differential equation of motion with derivative estimates made using finite-window filters. This inversion method is termed algebraic inversion of the differential equation (AIDE).

## THEORY

### Differential Equation of Mechanical Motion

The central hypothesis of this work is that mechanical properties can be obtained by direct inversion of a differential equation of motion using local polynomial fits to the data. It is therefore appropriate to describe the differential equation assumed. MRE deals with data that are proportional to the displacement of material isochromats, or spin-regions, suggesting the use of a Lagrangian, or material, coordinate system when considering the equations of motion.

A material coordinate system,  $\mathbf{a}$ , can be defined by considering a continuous region of moving material whose motion can be characterized by the vector-valued function describing displacement:

$$\mathbf{r}(\mathbf{a}, t) = \mathbf{a} + \boldsymbol{\xi}(\mathbf{a}, t)$$

where, for convenience,  $\boldsymbol{\xi}(\mathbf{a}, 0) = \mathbf{0}$  so that  $\mathbf{r}(\mathbf{a}, t)$  gives the position at time  $t$  of the point-mass that was at position  $\mathbf{a}$  at time  $t = 0$ .

<sup>1</sup>Ultrasound Research Laboratory, Mayo Foundation, Rochester, Minnesota.

<sup>2</sup>Biomathematics Resource Center, Mayo Foundation, Rochester, Minnesota.

<sup>3</sup>Magnetic Resonance Imaging Laboratory, Mayo Foundation, Rochester, Minnesota.

Grant sponsor: NIH; Grant numbers: CA75552; HL61451.

\*Correspondence to: James F. Greenleaf, 200 First Street SW, Mayo Foundation, Rochester, MN 55905.

Received 20 March 2000; revised 30 August 2000; accepted 11 September 2000.

© 2001 Wiley-Liss, Inc.

Conservation of momentum provides the dynamic equation of motion relating material properties to displacement. Define the components of  $\text{DIV } \mathbf{P}(\mathbf{a}, t)$  to be the divergence with respect to the material coordinate system of the (row) components of  $\mathbf{P}$ . Ignoring body forces, momentum conservation written in a Lagrangian coordinate system is (13)

$$\rho_0(\mathbf{a}) \frac{\partial^2}{\partial t^2} \boldsymbol{\xi}(\mathbf{a}, t) = \text{DIV } \mathbf{P}(\mathbf{a}, t)$$

where

$$\mathbf{P}(\mathbf{a}, t) = \boldsymbol{\sigma}^L(\mathbf{a}, t) \det \left( \mathbf{I} + \frac{\partial \boldsymbol{\xi}}{\partial \mathbf{a}} \right) \left( \mathbf{I} + \frac{\partial \boldsymbol{\xi}}{\partial \mathbf{a}} \right)^{-1}.$$

$\boldsymbol{\sigma}^L(\mathbf{a}, t) \equiv \boldsymbol{\sigma}(\mathbf{r}(\mathbf{a}, t), t)$ , and  $\boldsymbol{\sigma}(\mathbf{r}, t)$  is the Cauchy stress tensor describing internal forces that arise due to the strain of the material. Additionally,  $\rho_0(\mathbf{a}, t)$  is the initial (reference) density of the material and the displacement-gradient matrix is defined so that  $(\partial \boldsymbol{\xi} / \partial \mathbf{a})_{ij} \equiv \partial \xi_i / \partial a_j$ . The tensor  $\mathbf{P}(\mathbf{a}, t)$  is called the first Piola-Kirchhoff stress tensor (13). It is evident that these equations are non-linear in general.

The goal of elastography is to make useful characterizations of the constitutive relationship between the stress tensor and material displacement. Practically, this means assuming a material model and estimating parameters of that model from the data. While biomaterials exhibit a range of constitutive equations (14), for simplicity we assume the tissue of interest can be well modeled as a linear, Hookean, viscoelastic solid. Under several viscoelastic models (such as Voigt, Maxwell, and Kelvin), a linear relationship between stress and displacement can be written in the temporal Fourier domain as

$$P_{ij}(\mathbf{a}, f) = C_{ijkl}(\mathbf{a}, f) \Xi_{kl}(\mathbf{a}, f) \quad [1]$$

where  $C_{ijkl}(\mathbf{a}, f)$  is a complex stiffness tensor with 2–36 independent elements depending on the symmetry of the material. To estimate  $C_{ijkl}$  in the most general linear case, three sets of phase-difference data must be collected, each with sensitization in one of the Cartesian directions and a changing time offset between the displacement and the gradients so that a phase-difference time-series is collected. If we define  $\Phi_i(\mathbf{a}, f)$  to be the Fourier transform of the time-series collected with motion-encoding in the  $i$ th direction, the entire phase-difference data set can be directly related to the stiffness tensor with the equation

$$-(2\pi f)^2 \rho_0(\mathbf{a}) \Phi_i(\mathbf{a}, f) = [C_{ijkl}(\mathbf{a}, f) \Phi_{kl}(\mathbf{a}, f)]_i \quad [2]$$

due to the proportional relationship between the phase-difference dataset,  $\Phi_i$  and the displacement  $\Xi_i$  (15).

In principle, it is possible to use measurements of displacement to find all components of the stiffness tensor  $C_{ijkl}(\mathbf{a}, f)$ . For simplicity, only isotropic materials will be considered here. In an isotropic material the stiffness tensor is unchanged under arbitrary rotation of the coordinate axes. In other words, the response of the material does not depend on the orientation of the disturbance. At millimeter scales this description applies to many soft tissues such

as breast, liver, and prostate, but the description is less applicable for other tissues such as muscle and bone. How limiting the isotropic assumption is for tumors has yet to be determined, although one author suggests that tumors should be modeled as anisotropic (16).

In isotropic materials, symmetry constraints reduce the 36 independent coefficients in  $C_{ijkl}$  to two Lamé constants,  $\Lambda$  and  $M$  (written here in capital letters for consistency with the Fourier-domain notation):

$$C_{ijkl} = \Lambda \delta_{ij} \delta_{kl} + M(\delta_{ik} \delta_{jl} + \delta_{il} \delta_{jk})$$

where  $\delta_{ij}$  is the Kronecker delta which is zero unless  $i = j$  when it takes the value of one. Other parameters which are commonly used to quantify stiffness such as Young's modulus,  $E$ , the bulk modulus,  $K$ , shear modulus,  $G$  ( $\equiv M$ ), and Poisson's ratio,  $\nu$ , can all be defined in terms of these coefficients (17).

Using the Lamé coefficients in Eq. [2] one can write a small-amplitude, broadband, harmonic equation of motion for isotropic materials:

$$-(2\pi f)^2 \rho_0(\mathbf{a}) \Phi_i(\mathbf{a}, f) = [\Lambda(\mathbf{a}, f) \Phi_{jj}(\mathbf{a}, f)]_i + [M(\mathbf{a}, f) \times (\Phi_{ij}(\mathbf{a}, f) + \Phi_{ji}(\mathbf{a}, f))]_i \quad [3]$$

This is the partial differential equation assumed for broadband, source-free, small-amplitude motion in an isotropic, viscoelastic material, with displacement replaced by appropriately collected phase-difference data.

#### Estimation of Lamé Constants

Our method, AIDE, consists of inverting Eq. [3] by assuming *local* homogeneity to transform it into an algebraic equation applicable at each spatial position,  $\mathbf{a}$ , and temporal frequency,  $f$ .

$$\mathbf{A} \begin{bmatrix} \Lambda(\mathbf{a}, f) + M(\mathbf{a}, f) \\ M(\mathbf{a}, f) \end{bmatrix} = -4\pi^2 f^2 \rho_0(\mathbf{a}) \begin{bmatrix} \Phi_1(\mathbf{a}, f) \\ \Phi_2(\mathbf{a}, f) \\ \Phi_3(\mathbf{a}, f) \end{bmatrix} \quad [4]$$

where

$$\mathbf{A} = \begin{bmatrix} A_{11} & A_{12} \\ A_{21} & A_{22} \\ A_{31} & A_{32} \end{bmatrix} = \begin{bmatrix} \Phi_{i,11}(\mathbf{a}, f) & \Phi_{1,i1}(\mathbf{a}, f) \\ \Phi_{i,i2}(\mathbf{a}, f) & \Phi_{2,ii}(\mathbf{a}, f) \\ \Phi_{i,i3}(\mathbf{a}, f) & \Phi_{3,ii}(\mathbf{a}, f) \end{bmatrix},$$

and repeated indices imply a sum from 1 to 3.

This expression can be inverted to obtain an estimate of the complex Lamé coefficients for each position and temporal frequency contained in the phase-difference data.

$$\begin{bmatrix} \Lambda(\mathbf{a}, f) + M(\mathbf{a}, f) \\ M(\mathbf{a}, f) \end{bmatrix} = -4\pi^2 f^2 \rho_0(\mathbf{a}) \times (\mathbf{A}^H \mathbf{A})^{-1} \mathbf{A}^H \begin{bmatrix} \Phi_1(\mathbf{a}, f) \\ \Phi_2(\mathbf{a}, f) \\ \Phi_3(\mathbf{a}, f) \end{bmatrix} \quad [5]$$

In this expression,  $\mathbf{A}^H$  denotes the conjugate transpose of the matrix  $\mathbf{A}$ . A full expression for Eq. [5] is given in the

Appendix. The equation assumes that we know the density of the material. If the density is unknown, we can only estimate the ratio of shear modulus to density using AIDE. However, density variations in soft-tissue are small, which allows the reasonable assignment of  $\rho_0 = 1000 \text{ kg/m}^3$  in most cases (since tissues are largely composed of water).

### Two-Dimensional Inversion

As it is useful to compare algorithms assuming 2D data, we note that to obtain a 2D version of Eq. [5], set all derivatives in the  $z$  direction ( $i = 3$ ) to zero. This implies that  $A_{31} = 0$  and sums run from 1 to 2 in the remaining elements of  $\mathbf{A}$ . Under this assumption, the equations decouple into two independent, 2D modes. Each mode can be used to find  $M(\mathbf{a}, f)$  independently. Alternatively, both modes may be used in an effort to improve estimate quality. The simplest inversion scheme occurs with measurements of the out-of-plane shear mode for a purely 2D problem. In this case

$$M(\mathbf{a}, f) = \frac{-4\pi^2 f^2 \rho_0(\mathbf{a}) \Phi_3(\mathbf{a}, f)}{\Phi_{3,11}(\mathbf{a}, f) + \Phi_{3,22}(\mathbf{a}, f)}. \quad [6]$$

In elastography of soft tissues  $\mu/\lambda$  is very small ( $\approx 0.0001$ ), which creates difficulties in trying to reliably estimate both Lamé coefficients from  $\Phi_i$  using Eq. [3]. As a result, we must guess at a value of  $\Lambda$  to use, estimate  $\Lambda$  as a “nuisance” parameter and ignore it, or somehow obtain an expression that relates  $\Phi_i$  to  $M$  alone. We use the latter two approaches in this work, and two different methods for eliminating  $\Lambda$  from the differential equation.

### Inversion by Neglecting Longitudinal Component

One method to obtain a relationship between displacement (phase-difference) and shear modulus alone is to ignore the term in Eq. [3] that involves  $\Lambda$ . This means assuming that  $\Lambda \nabla \cdot \Phi$  (which can be interpreted as a hydrostatic pressure under an incompressibility assumption) is constant in space. With the large differences in wavelength between longitudinal and shear waves at frequencies relevant to medical elastography, this is not a restrictive assumption to make. With this assumption, Eq. [4] becomes

$$\begin{bmatrix} A_{11} + A_{12} \\ A_{21} + A_{22} \\ A_{31} + A_{32} \end{bmatrix} M(\mathbf{a}, f) = -4\pi^2 f^2 \rho_0(\mathbf{a}) \begin{bmatrix} \Phi_1(\mathbf{a}, f) \\ \Phi_2(\mathbf{a}, f) \\ \Phi_3(\mathbf{a}, f) \end{bmatrix}.$$

The least-squares solution to this over-determined system of equations is

$$M(\mathbf{a}, f) = -4\pi^2 f^2 \rho_0(\mathbf{a}) \times \frac{(A_{11} + A_{12})^* \Phi_1 + (A_{21} + A_{22})^* \Phi_2 + (A_{31} + A_{32})^* \Phi_3}{|A_{11} + A_{12}|^2 + |A_{21} + A_{22}|^2 + |A_{31} + A_{32}|^2}. \quad [7]$$

Note that we still need to measure all three polarizations of phase-difference (three sensitization directions) to obtain

an estimate for the complex shear Lamé coefficient using this model.

### Incompressible (Helmholtz) Inversion

If, rather than simply neglecting variations associated with the longitudinal wave,  $[\Lambda(\mathbf{a}, f) \Phi_{j,j}(\mathbf{a}, f)]_{,i} = 0$ , we assume full incompressibility,  $\Phi_{j,j} = \nabla \cdot \Phi = 0$ , then  $A_{i1} = 0$ , and the equations of motion decouple into three separate expressions for shear modulus. This allows measurement of a single sensitization direction to produce an estimate for  $M$  by inverting the Helmholtz equation (Helmholtz inversion):

$$M(\mathbf{a}, f) = -4\pi^2 f^2 \rho_0(\mathbf{a}) \frac{\Phi_i(\mathbf{a}, f)}{\Phi_{i,11}(\mathbf{a}, f) + \Phi_{i,22}(\mathbf{a}, f) + \Phi_{i,33}(\mathbf{a}, f)}. \quad [8]$$

### Speed and Attenuation

Equations [5]–[8] demonstrate that the algebraic inversion method returns the ratio of stiffness to density. The real and imaginary parts of this ratio can be used to compute shear wave speed and attenuation with the formulas:

$$c_s(f) = \sqrt{\frac{2(M_{\rho R}^2 + M_{\rho I}^2)}{(M_{\rho R} + \sqrt{M_{\rho R}^2 + M_{\rho I}^2})}} \quad [9]$$

$$\alpha(f) = \sqrt{\frac{(2\pi f)^2 (\sqrt{M_{\rho R}^2 + M_{\rho I}^2} - M_{\rho R})}{2(M_{\rho R}^2 + M_{\rho I}^2)}} \quad [10]$$

where we have defined  $M_{\rho R}$  and  $M_{\rho I}$  to be, respectively, the real and imaginary parts of  $M/\rho$ . The wave speed and wave attenuation values provide the same information as the ratio of complex-valued stiffness to density, and these are the values that will be reported in the Results section.

The estimation procedure can be carried out for each frequency with significant amplitude in the collected dataset to obtain frequency-dependent estimates of the shear wave speed and loss parameter. In addition, the longitudinal wave speed and attenuation may be obtained from  $\Lambda$  using these same two equations by replacing  $M$  with  $\Lambda + 2M$ .

## METHODS

### Data Generation

To test the hypothesis that complex-valued Lamé constants can be estimated from a direct algebraic inversion of the differential equation of motion, we generated a computer-simulated displacement dataset. We also acquired two real displacement datasets with tissue-simulating phantoms using the MRE technique that has been previously described (1,8).

### Simulated Data

The simulated dataset was generated by analytically solving Eq. [3] for two half-spaces with an incident plane-wave in the left-hand side traveling at an angle of  $24.5^\circ$  and

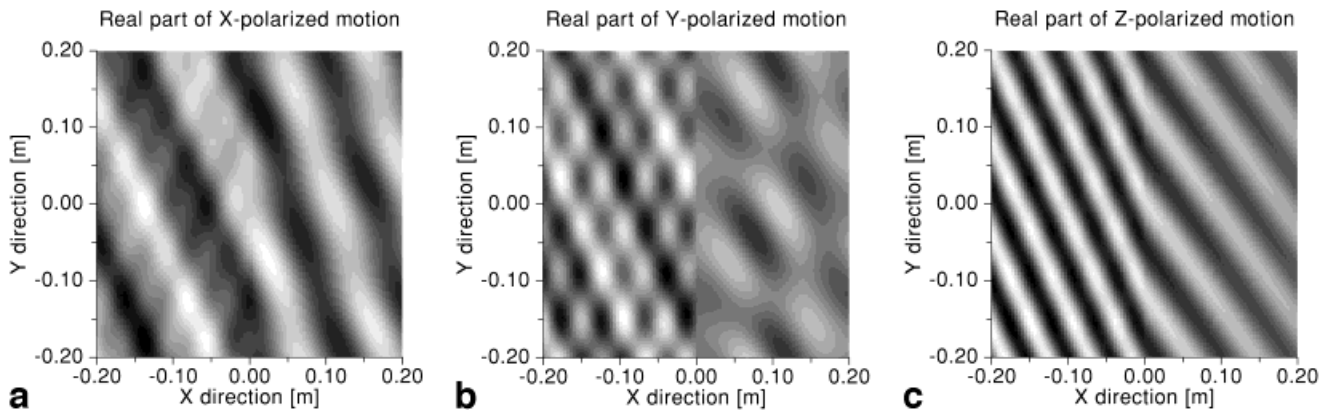


FIG. 1. Real part of each polarization of harmonic motion resulting from a plane-wave impinging on boundary at an angle of 24.5°.

containing all of the fundamental modes with relative amplitudes of 0.5 for the vertical shear mode, 0.25 for the horizontal shear mode, and 1.0 for the longitudinal mode. The amplitude and direction of the reflected and transmitted waves were found by enforcing continuity of displacement and continuity of force at the boundary between the materials. The details of the calculation to obtain the total field given the material parameters and the incident-wave direction and modal amplitudes are available in many textbooks (see Ref. 17 for example). To demonstrate the possibility of reconstructing the longitudinal coefficients in certain materials, the material coefficients were artificially selected so that the shear and longitudinal wave speeds were similar. Specifically, we selected 40 m/sec, 15 m/sec, 0.5 Np/m, and 1.0 Np/m as the longitudinal wave speed, shear wave speed, longitudinal attenuation, and shear attenuation, respectively, for the left half-space. The right half-space material coefficients were set respectively to 30 m/sec, 21 m/sec, 1.0 Np/m, and 3.0 Np/m. The frequency used for simulation was 300 Hz. All polarizations of motion for the real part of the generated harmonic field are shown in Fig. 1. To demonstrate the effect of noise on the reconstructions, we also created a dataset by adding to the simulated data zero-mean Gaussian noise with a standard deviation of 20% of the maximum displacement value.

To produce a 3D field for use with the 3D AIDE algorithm, the inherently 2D analytic solution is assumed to be equivalent in each slice in the out-of-plane direction.

#### Experimental Phantom Data

Two 3D, experimental displacement datasets were generated using trapezoidal multi-axis motion-encoding gradients with a 3D, spin-warp image encoding sequence as described in Refs. 1, 8, and 18. The TR and TE times were 100 and 20 msec, respectively, and the flip angle was 30°. The multi-axis encoding was accomplished using a tetrahedral sensitization strategy (19) that requires four independent views of the region: one reference view encodes motion along all Cartesian axes while the other three views each reverse the polarity of the motion-encoding gradient along one of the axes. Subtracting the phase of one of the last three views from the phase of the reference view gives

the phase-difference data for one sample time. Eight phase-offsets between the applied mechanical waves and the motion-encoding gradient waveform were gathered, covering one period of the applied cyclic motion. This produced a time-series for each position from which  $\Phi_i(a, f)$  was estimated as the first harmonic of the discrete Fourier transform.

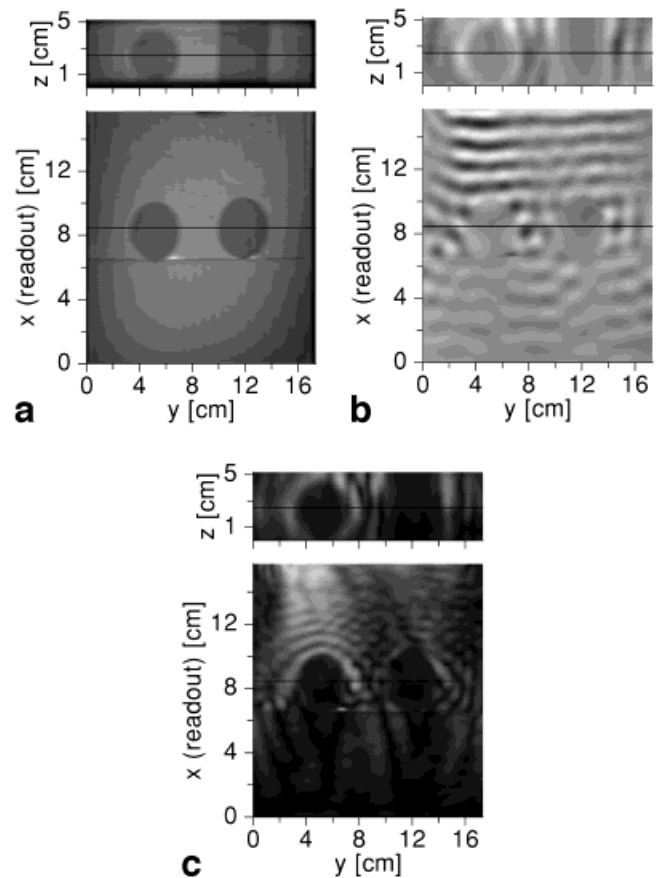


FIG. 2. 3D datasets visualized with two orthogonal views connected at the horizontal line in each view: (a) average magnitude, (b) phase-difference sensitized to the z-direction for one time-offset, and (c) vector-magnitude at vibration frequency (300 Hz):  $\sqrt{|\Phi_1|^2 + |\Phi_2|^2 + |\Phi_3|^2}$ .



The first phantom consisted of a sphere and a cylinder constructed from 3.0% agar gel inside a block of 1.5% agar gel. The field of view (FOV) was  $24 \times 24 \times 30$  cm, and shear motion was applied in the  $z$  direction to the surface of the phantom, with a 300 Hz sinusoidal signal triggered by the pulse sequence as described in Refs. 1 and 8. Figure 2a shows two orthogonal slices of the (MR) magnitude data obtained by averaging all 32 of the time-offsets and motion-sensitizations ( $8 \times 4$ ) of the full dataset. The reconstruction technique presented in this work inherently assumes that the material is moving at each reconstructed point in an image. Attenuation and standing waves can produce regions that do not move much at all, resulting in poorly-interrogated image locations. To get an idea of the motion of the material at 300 Hz, Fig. 2b presents two orthogonal views of the difference data sensitized to the  $z$ -direction for a particular offset between the motion and the motion-sensitizing gradients. Figure 2c shows the same views of the (vector) magnitude of the 300 Hz component of the Fourier transform of the phase-difference dataset.

The second phantom was used to test the performance of reconstructions for a stiff inclusion near a material edge. It consisted of a small ellipsoid of 3.0% agar gel at the edge of a block of 1.5% gel. The FOV was  $8 \times 8$  cm and the phantom was vibrated in the  $z$ -direction with a 400 Hz sinusoidal waveform triggered by the pulse sequence. Figure 3 shows two orthogonal views of several presentations of the collected data: Fig. 3a shows the average MR magnitude image; Fig. 3b shows the phase-difference image for sensitization in the  $z$ -direction; and Fig. 3c shows the (vector) magnitude of the fundamental frequency. The latter figure can be used to identify poorly-interrogated regions where the motion-amplitude is low.

### Data Analysis

To find the complex-valued Lamé coefficients, Eq. [5] was evaluated point-by-point on a rectangular grid using harmonic data. The simulated dataset was generated in the temporal frequency domain. Harmonic data were obtained from the experimental data using the fast Fourier transform (FFT) on the time-offsets for each spatial position.

### Estimation of Spatial Derivatives

Eq. [5] requires values for the derivatives of the displacement which must be estimated from the noisy displacement data. We estimated derivatives using a least-square fitting procedure made popular by Savitsky and Golay (20). The data are fit to a separable polynomial in a fixed local window, and derivatives of the best-fit polynomial are used as estimates of the data derivatives. This fit-and-estimate-derivative procedure results in a linear filter that is potentially spatially-varying if regions near the boundary are given special consideration or if the window size is altered in the ROI. The order of the polynomial and the size of the local window can be specified. We have found that good results can be obtained using a second- or third-order polynomial fit (for symmetric windows these result in the same filter), where the window size is chosen to be less than one-half the expected wavelength. As a further

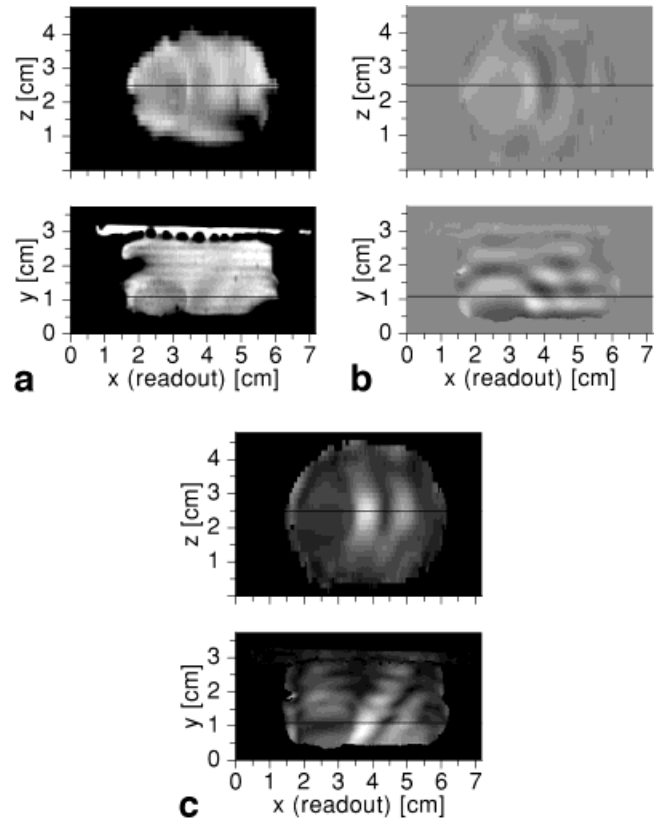


FIG. 3. 3D datasets visualized with two orthogonal views connected at the horizontal line in each view: (a) average MR magnitude, (b)  $z$ -sensitized phase-difference for one time offset, and (c) vector magnitude of fundamental mode:  $\sqrt{\Phi_1^2 + \Phi_2^2 + \Phi_3^2}$ .

noise-reduction step, the raw phase-difference data were filtered with a linear filter that has the effect of replacing the value at the center of a local window with the value of the best-fit polynomial.

### Regularization

Finding the complex Lamé coefficients using the AIDE approach ultimately requires the division of two numbers which can cause numerical difficulties if the denominator is near zero. Define *poorly-interrogated* regions as those whose displacement field result in a denominator that is nearly zero. In the presence of noise, the effect of poorly-interrogated regions is amplified. In the simplest case where we assume homogeneity and incompressibility it can be seen that poorly-interrogated regions correspond to regions where  $\nabla^2 \Phi_i(\mathbf{a}, f) \approx 0$  or  $\Phi_i(\mathbf{a}, f) \approx 0$ . The Helmholtz equation demonstrates that these two conditions are equivalent to within a scale factor in the (locally) homogeneous case. In order to regularize the solution we apply two independent methods: 1) project the real part of  $M(\mathbf{a}, f)$  onto non-negative numbers (zero-out negative results), and 2) apply a median filter which takes as the final output the median of the values in a local window.

## RESULTS

### Simulated Data

To verify the AIDE code and to demonstrate its performance in estimating all four coefficients (speeds and at-

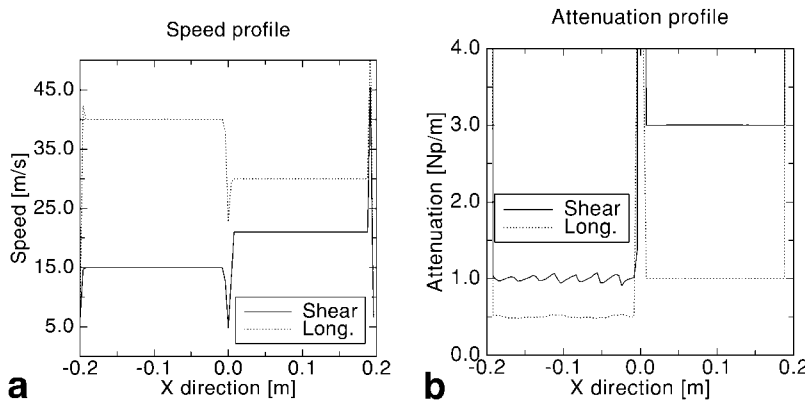


FIG. 4. Profile plots for the line  $y = 0.0$  in Fig. 1 showing AIDE reconstructions of shear and longitudinal wave speed (a) and attenuation (b). The maximum values of 310.9 Np/m for shear and 47.3 Np/m for full are clipped in b. See text for true values, which are nearly perfectly reconstructed away from material boundaries.

tenuations for the two types of waves), we generated a simulated dataset based on a single-frequency plane-wave solution to the isotropic equations of motion with a single boundary between two half-spaces. We applied full AIDE (Eq. [5]) to this 3D, three-polarization simulated dataset using separable polynomials of length 5 and order 4 (no noise-smoothing). Profiles for the line  $y = 0.0$  from the resulting reconstructions of wave speed and attenuation for both shear and longitudinal waves are shown in Fig. 4.

These figures demonstrate the viability of the proposed method, as the reconstructions away from boundaries are nearly perfect. The attenuation profiles do show variability in the left region even for this only-numerical-noise case. Near boundaries the method also shows difficulties in reconstructing the true values, likely due to the inherent homogeneity assumption.

To evaluate the noise sensitivity of the estimates of shear and attenuation, we added 20% noise to each of the polarizations of motion. Figure 5 shows profiles of the line  $y = 0.0$  for both shear speed and attenuation using several versions of the AIDE algorithm: full-inversion (Eq. [5]), 3D incompressible using z-polarized motion (Eq. [8]), and 2D incompressible using z-polarized motion in each plane in a slice-by-slice fashion (Eq. [6]). In each case, polynomial filters of size 11 in-plane and size 5 out-of-plane were used, and the final median filter had a kernel size of  $3 \times 3 \times 3$ .

Figure 5 suggests that the variance of the shear speed estimate is smaller and the edges are smoother when using the incompressible assumption, but the resulting estimate is biased for the region on the left. The attenuation profile

demonstrates the significant noise sensitivity of the attenuation estimate, especially for the full inversion case. Making the 2D assumption (which is valid for this example), helps the algorithm, allowing a qualitative assessment of attenuation, but the mean value in both regions is still higher than the true parameter. From these analytic results, we can expect some success in reconstructing quantitative shear speed given real MRE data, and can perhaps obtain some useful qualitative results regarding attenuation.

### Experimental Data

In the first experiment we test the assumptions which lead to less data-intensive versions of AIDE for a simple MRE imaging experiment by comparing several reconstruction methods. Given the mathematical description in Eq. [5], we expect AIDE reconstructions to perform best in regions where the amplitude of motion is highest. This hypothesis is substantiated by Fig. 6, which shows reconstructions of the phantom using three versions of the AIDE algorithm. These reconstructions were made with separable polynomial filters of order 2 with window sizes of 7 in the x-y plane and 5 in the z direction. A final median filter of order  $3 \times 3 \times 3$  ( $3 \times 3$ , 2D) was also applied to the speed and attenuation results.

Examination of Fig. 6 reveals that there are only minor differences between the full inversion using Eq. [5], the 3D incompressible inversion using Eq. [8], and the 2D slice-by-slice inversion using Eq. [6] for this dataset. A more quantitative demonstration of these differences is pre-

FIG. 5. Reconstruction profile plots of wave speed (a) and attenuation (b) from the line  $y = 0.0$  of Fig. 1 after addition of 20% noise to each component of the motion. The maximum values of 23.7 for 2D incompressible, 22.2 for 3D incompressible, and 41.3 for full inversion are clipped in b.

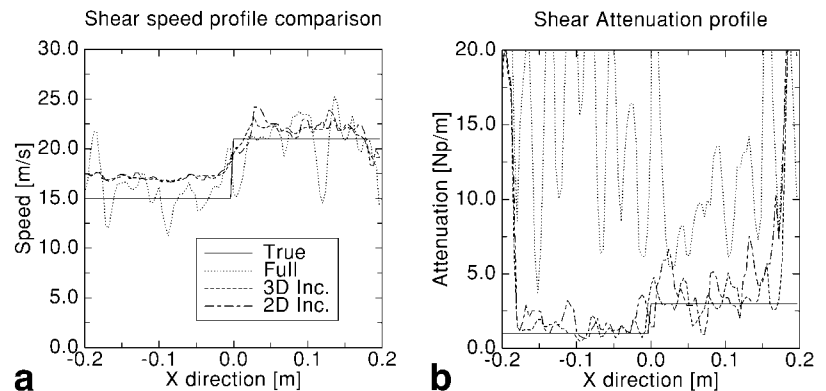
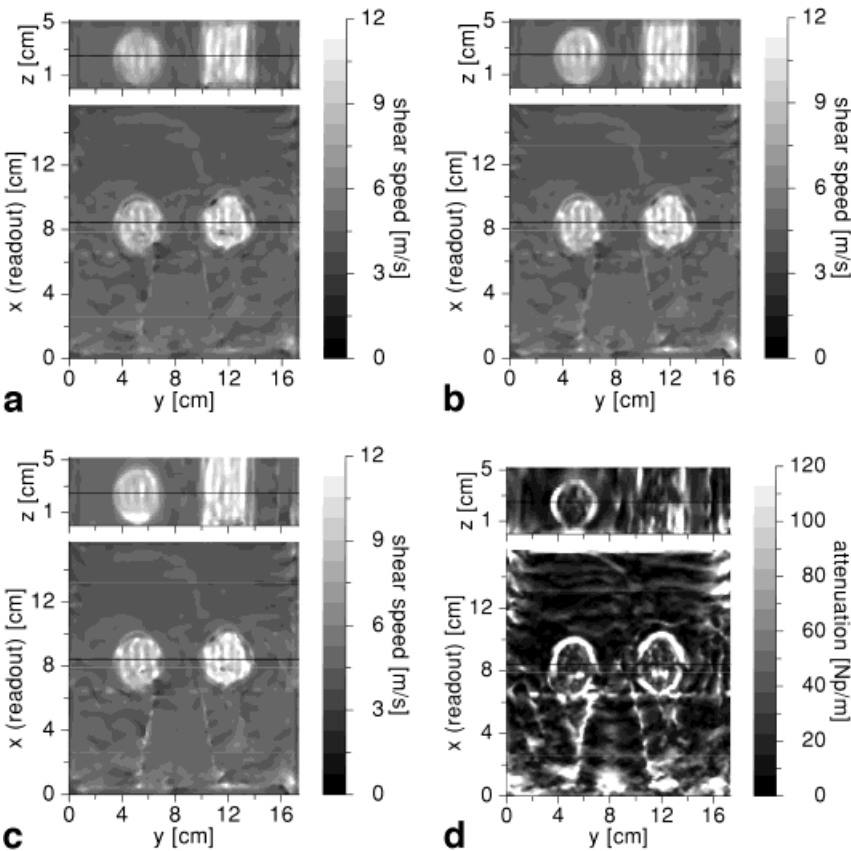


FIG. 6. 3D AIDE reconstructions of shear speed and attenuation for phantom 1 presented as two orthogonal views connected at the horizontal line shown in each view: (a) speed with no assumptions using all polarizations, (b) speed with incompressible assumption using only z-polarization, (c) speed with incompressible and 2D assumption using only z-polarization in each slice independently, and (d) attenuation with incompressible assumption using only z-polarization.



sented in Table 1. The shear speed images show the sphere and cylinder with good clarity even with the low amplitude of motion in the objects (which could be the source of much of the variability in the quantitative estimate). Some of the poorly-interrogated regions are also visible in the shear-speed images behind the sphere and cylinder in the x-y plane. The attenuation map shows the boundaries between materials very clearly (so that the inclusions can be identified) and also highlights the regions with small displacement. The minor differences between the recon-

struction methods for this dataset can be more clearly seen in a profile plot along the line connecting the two orthogonal views in Fig. 6. The quantitative shear speed profiles for all three reconstruction methods are shown in Fig. 7a. The profiles also emphasize the variability of the estimate inside the sphere and cylinder and the homogeneity of the reconstruction in the background region.

The MR magnitude image in Fig. 2a shows a bright region to the right and below the sphere in the x-y plane and a line separating the two gels (which results from the

Table 1  
Reconstruction Statistic for Regions of Interest in Each Data Set

	RVM	Full AIDE (m/s)			3D Helmholtz (m/s)			2D Helmholtz (m/s)			"True"
		Mean	SD	%	Mean	SD	%	Mean	SD	%	
Simulation											
Left	—	14.98	1.41	9.4	17.01	0.15	0.9	17.02	0.29	1.7	15.0
Right	0.78	21.6	1.87	8.6	21.99	0.71	3.2	22.04	1.55	7.0	20.0
Phantom 1											
Background	—	4.24	0.22	5.0	4.24	0.22	5.1	4.24	0.22	5.3	4.1
Cylinder	0.09	9.83	0.89	9.1	9.91	1.15	11.6	10.25	1.31	12.8	9
Sphere	0.09	8.70	0.92	10.6	9.08	1.10	12.2	9.10	1.18	12.9	9
Phantom 2											
Background	—	3.40	0.15	4.5	3.40	0.16	4.7	3.44	0.18	5.1	3.5
Inclusion	0.25	6.35	0.61	9.6	6.49	0.63	9.6	6.72	0.68	10.2	7.5

The mean, standard deviation (SD), and the ratio of standard deviation to the mean (as a %) in each region is presented for each of the three reconstruction methods used in the text. The first column gives the Relative Vector Magnitude (RVM) of the data in the region of interest with respect to the data in a reference region of interest in the same experiment. The "true" values are the known values in the simulation and the values for the phantoms measured using a different inversion technique as explained in the text. The units of all quantities except percentages are in m/s.

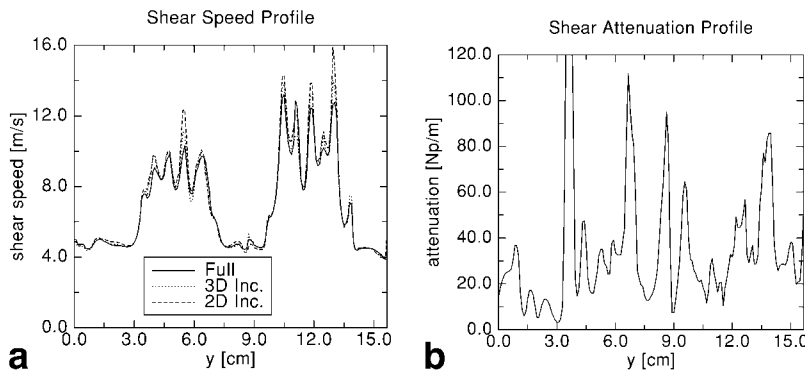


FIG. 7. Comparison of shear speed (a) and attenuation (b) values along the line joining the two orthogonal views presented in Fig. 6. The attenuation plot in b shows only the results from the 3D incompressible calculation (the other methods give similar results) and clips the maximum of 169.6.

layers being poured at separate times). This line is also visible in the reconstructed speed images as a stiffer material, though this is likely only a boundary artifact. There is also a softer material visible to the right and below the sphere in the  $x$ - $y$  plane of the reconstructed speed images that correlates with a bright spot in the same location in the MR magnitude image in Fig. 2a.

The results of the attenuation estimates are presented in Figs. 6d and 7b. Figure 6d shows two orthogonal views for 3D incompressible reconstructions, while the profile along the view-intersection line is shown in Fig. 7b. The image clearly shows the boundaries of the sphere and cylinder in addition to the line separating the background gels as likely boundary artifacts. The profile mirrors the significant variability seen in the attenuation reconstructions of the noisy simulated data.

Results from the second experimental phantom are shown in Figs. 8 and 9. Figure 8 shows 3D, incompressible AIDE reconstructions using the  $z$ -polarization of a portion of the FOV. Both images were constructed using separable second-order polynomial filters of length 13 in the  $x$ - $y$  plane and length 3 in the  $z$ -direction. A final median filter of size  $3 \times 3 \times 3$  ( $3 \times 3$  in 2D) was also applied. The quantitative shear-speed values from this phantom are smaller than the reconstructed values from the first phantom in both the 1.5% gel and the 3.0% gel, suggesting softer gels.

The speed image shows good contrast between the inclusion and the background, but the inclusion appears smaller in the reconstructed speed image than it does in the MR magnitude image. Most of this size reduction can be attributed to the inclusion sitting so close to the material edge. Because derivatives are calculated using mea-

surements of the phase-difference data in a local window, boundary effects due to lack of data will occur near image edges. This lack-of-data problem could be addressed by using skewed rather than symmetric data windows to estimate derivatives near material-edge boundaries. Nonetheless, the boundary of the inclusion is more accurately depicted by the reconstruction of shear attenuation (along with regions of low motion). Quantitative profiles of the reconstructed phantom are shown in Fig. 9. The speed reconstructions show much smaller variability in the background gel than in the stiff inclusion. We suspect that this is in part due to the decreased amplitude of motion in the stiff inclusion.

Table 1 provides a quantitative summary of the simulation and experimental shear wave-speed results of the AIDE algorithms using Savitsky-Golay derivative filters. To construct this table, ROIs were first manually selected from the 3D data reconstructed using full AIDE inversion, 3D incompressible AIDE, and 2D slice-by-slice reconstruction. The sample mean, sample standard deviation, and the ratio between the standard deviation and the mean are presented for each of the selected regions and the three main reconstruction methods. Also included in the table is the relative vector magnitude (RVM) of the vector displacement values in the selected region. This is defined as the ratio of the squared vector magnitude of the displacement (phase-difference) data to the same quantity in a reference region in the same dataset. We expect the standard deviation of the reconstructed estimates to increase with decreasing vector displacement magnitude. The “true” values reported in the final column of the table represent approximations to the shear-wave speed found by independent methods. For the simulations, the column

FIG. 8. 3D shear speed and attenuation for phantom 2 reconstructed using AIDE and visualized with two orthogonal views connected by the horizontal line shown.

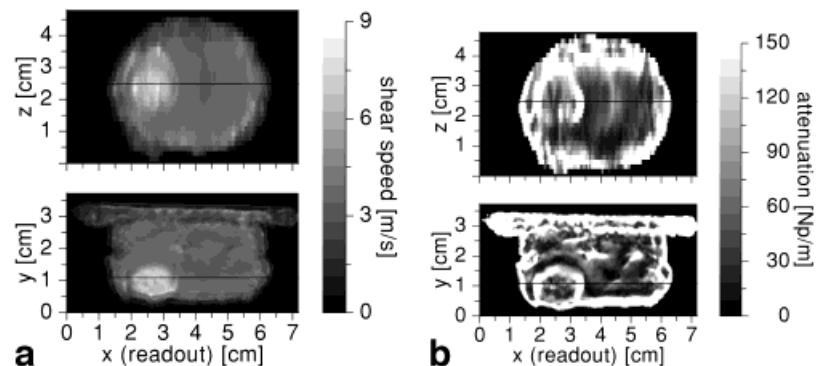
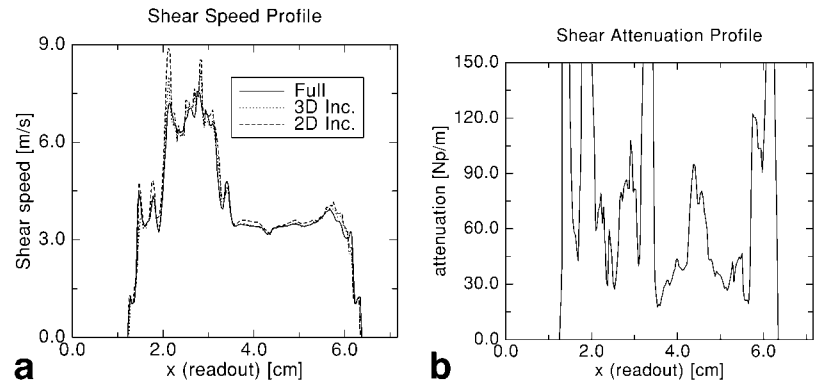




FIG. 9. Profiles along the line joining the two views shown in Fig. 8 using 3D, incompressible AIDE on the z-polarized motion. For reference, **a** compares results from full inversion and 2D slice-by-slice inversion, while **b** only includes 3D incompressible results (the other methods give similar results) and clips the maximum of 1729.7.



holds the actual true values. For the sphere-cylinder phantom, the column holds estimates of the shear speed found by averaging 10 manual approximations to the wavelength found by using an interactive image tool. For the edge-inclusion phantom, the “true” background shear-wave speed was found by taking the square root of the shear-modulus-divided-by-density found using the local-frequency estimator as explained in Ref. 21. The “true” value for the inclusion was found by taking the square root of the shear-modulus-divided-by-density computed using a local-frequency estimate with another homogeneous phantom made from the same gel mixture.

## DISCUSSION

The results of the simulation and phantom studies confirm our hypothesis that quantitative estimates of material properties can be obtained from dynamic measurements of internal displacement using direct, local inversion of the differential equation of motion with derivative estimates made using finite-window filters.

### Speed Reconstructions

The results indicate that AIDE can be used to estimate both shear and longitudinal wave speeds provided their values are similar so that longitudinal and transverse motions occur on the same spatial scale. In tissue-like material, in which shear wavelength is much shorter than longitudinal wavelength, it is only possible to reconstruct one or the other. For acoustic frequencies, shear speed can be reconstructed from displacement data using direct inversion of the equation of motion. The variability in the reconstructions in homogeneous regions correlates with the total amplitude of motion in those regions, which is consistent with Eqs. [5]–[8]. Using Savitsky-Golay filters for the derivative estimation can introduce a bias in the resulting estimates (especially in regions of low shear wave-speed) due to the inability of a polynomial to model a sinusoid for large window-size-to-wavelength ratios. Although such biases can occur, the large bias present in the noisy simulations in Fig. 1 is more likely a result of the fact that the simulation is not incompressible and therefore does not satisfy a local Helmholtz equation. This conjecture is supported by the decreased bias in the estimate which uses full AIDE reconstruction.

Estimating derivatives from noisy data, as is done in this work, is sometimes viewed as an unstable activity, primarily due to the inappropriate use of applying first-differences to raw data. However, derivatives can be stably estimated in practice by filtering the data with the derivative of a low-pass filter, which is done here through the use of Savitsky-Golay filters. As evidenced by the simulation reconstructions using 3D Helmholtz inversion, this practice can provide derivative-based estimates of shear-wave speed with less than 4% variability despite the presence of 20% noise on the input data.

The homogeneity assumption induces edge-enhancing artifacts in the reconstructed speed in the noise-free case. When noise is added, sharp edges in speed data are reconstructed as comparably smooth transitions, which implies that for the cases presented, the systematic “model-noise” due to the imperfect model is not as important as the measurement noise. However, reconstructions in attenuation maintain their edge-enhancing property despite the addition of noise, as evidenced by the phantom reconstructions.

For the illuminations considered in the phantom, 2D, slice-by-slice reconstructions of shear speed do not differ significantly from reconstructions obtained by inverting the full 3D, three-polarization differential equation. This equivalency between 2D and 3D results will not likely hold for more complicated insonifications, which produce waves traveling in oblique directions.

From the equations and data presented, we propose that the major difficulty in effective application of this technique to tissue is in inducing adequate motion in stiff ROIs. This is due to the essential trade-off between variability in the resulting output and resolution. The higher the displacement in a particular region (for a given constant phase variability due to noise in the imaging process), the lower the resolution can be for a given acceptable level of output variability. Table 1 demonstrates this statement, as the regions with lower displacement consistently have higher output variability. Given these considerations, we speculate that methods which either increase the magnitude SNR (and correspondingly decrease the phase variability) or increase the amount of displacement in an ROI will improve image quality as measured by resolution and variability.

## Attenuation Reconstructions

With AIDE it is possible to produce estimates of the complex-valued Lamé constants from which attenuation coefficients can be calculated. The results presented in this work indicate that attenuation images may be moderately useful in that stiffness boundaries are significantly enhanced in regions of adequate motion; however, quantitative values are unreliable using the same window sizes that give good results for speed estimates.

The poor relative performance of the attenuation estimates can be explained by noting that the attenuation is estimated by analyzing the displacement in a local window only. Attenuation causes an exponential decay on the underlying sinusoid. If the exponential decay is small over the window size, then this decay will be swamped by noise in the image, resulting in poor attenuation reconstructions. The smaller the attenuation, the smaller the variation over the window, and the worse the attenuation reconstruction will be for a fixed window size. With increased attenuation, however, there is less motion in deeper layers of the material, which makes reconstruction of both attenuation and speed more sensitive to noise. As a result, reconstruction of inhomogeneous attenuation images is difficult using AIDE. However, the method can potentially be used for homogeneous tissue attenuation characterization, an area for which little data exists in the literature.

## Relation to Other Methods

Several approaches for processing MRE data to obtain elasticity images have been proposed (10,11). The following paragraphs briefly compare some of these approaches to the AIDE technique.

### *Local Frequency Estimate (LFE)*

The first general approach to estimating stiffness from MRE data was to make use of an algorithm to generate local frequency estimates (LFEs), such as the one described in Ref. 21 and demonstrated on MRE data in Ref. 8. The LFE returns an estimate of local wave-number using a sequence of log-normal filters, with the property that the output of the next filter in the sequence is proportional to the spatial-derivative of the output of the previous filter. This approach treats the problem as an image-processing problem separate from the physics of mechanical motion. As a result, it is not immediately clear what aspects of the LFE make it applicable to data that satisfies the physics of general motion. This is one of the reasons that MR data collection intended for stiffness reconstruction has emphasized obtaining obviously-propagating strain waves which can be reconstructed using an image-processing technique. The results of this study indicate that the important factor is over-all motion at each image point, which suggests that the more complicated the motion the better. To summarize, AIDE provides a direct method like the LFE, but it is physically-based, which allows reconstruction of attenuation and shear modulus for any displacement field that locally satisfies the homogeneous equations of motion.

## *Variational Method*

The AIDE technique is a direct solution of the strong form (derivative form) of the dynamic differential equation including attenuation. Previously, other authors have suggested using the weak (variational, integral) form of the differential equation and appropriately chosen “test functions” to estimate both Lamé coefficients (10). Their method, which we call the variational method (VM), could be adapted to find only the shear modulus using the methods suggested here. It is also a straightforward extension of their method to estimate attenuation in a manner similar to what is done here.

The variational method avoids derivative calculations by taking analytic derivatives of test functions and integrating these over local windows in product with the data. The technique presented here, however, calculates derivatives in a similar but more general way (by filtering with the derivative of a smooth polynomial). An additional feature of the variational interpretation also allows selection of test functions which are zero on the boundary of a local region in order to eliminate the inhomogeneity from the problem. However, the modulus/density ratio is also assumed to be constant over this local-volume region, which is typically on the order of a wavelength. This is very similar to the assumption of piecewise-homogeneity given here that results in the Eq. [4]. Thus, the variational derivation, while providing valuable alternative insights into the problem, results in a very similar algorithm that can be viewed from the perspective of this work as using a particular method of computing local derivatives of the data.

### *Overlapping Subzone Technique*

Recently a technique was proposed to invert the full partial differential equation using Newton’s method to minimize the difference between measured displacement and displacement calculated using finite elements and a Young’s modulus estimate with an assumed Poisson ratio (11). This method has shown good results on synthetic data sets. The main difference between AIDE and this overlapping subzone technique (OST) is that AIDE is a direct technique while OST is an indirect one. As a result, AIDE may be computationally faster, and can provide 3D reconstructions of both shear speed and attenuation. In addition, although the technique could be straightforwardly adapted, the OST technique requires measurement of all displacement polarizations because no provision is described for assumptions that could lead to using only data from one polarization. Furthermore, the physical equations of motions assumed in Ref. 11 (for inhomogeneous parameters) and used in the inversion are slightly different from Eq. [3].

### *Insonification*

One aspect of the recent reconstruction methods (AIDE, VM, and OST) that should be re-emphasized is that since they do not rely on an image-processing technique but attempt to relate displacement to stiffness through a physical model, they do not depend on single plane-wave shear illumination. The only restriction on the methods is the

presence of motion (that satisfies the assumed model) in the ROI. In particular, complex interference patterns from reflections are not an issue except in regions where such patterns create areas of low amplitude, thereby lowering the SNR. In fact, these methods could benefit from increased complexity and amplitude of motion in the ROIs, where it serves to increase the total signal available for inferring mechanical properties. Much of the experimental data currently being collected (including the data in this work) are obtained using single plane-wave insonification, which often results in poorly-interrogated regions in which motion is limited.

### Resolution

The resolution of this reconstruction method is dependent on the window size used in estimating spatial derivatives over which the material is assumed to be homogeneous. The window size needed to get good signal in the resulting image is fundamentally noise-dependent, not shear-wave-length dependent, so reconstruction of sub-shear-wave-length is possible in principle. On the other hand, longer wavelengths mean less variation across the window and a smaller SNR in the derivative estimates, so there is an indirect relationship to wavelength.

### Extension to Inhomogeneous Equation of Motion

Assuming local homogeneity over a fixed window size allows writing the differential equation of motion as an algebraic equation. This assumption allows for very fast point-by-point processing that produces reasonable results for fully 3D data. Together with an incompressibility assumption, assuming local homogeneity also allows for a Helmholtz inversion that is less data intensive. If the assumption of homogeneity is removed then, even with an incompressibility assumption, it is apparent from Eq. [3] that using all polarizations of motion remains necessary except in a strictly 2D problem. The practical necessity of including other directions of motion is undoubtedly a function of stiffness differences and boundary conditions, and remains an open question.

### CONCLUSIONS

In this work a general framework for understanding methods for estimation of the material equation of state from internal displacement measurements has been presented. An algebraic inversion approach, AIDE, was developed for solving the strong form of the governing differential equation for linear, isotropic, “locally” homogeneous materials using local derivative filters. It was found that for tissue-like materials with a large difference between the propagation speeds of longitudinal and shear waves, an incompressibility assumption reduces data collection requirements without significantly altering reconstructed values. Results from simulated and experimental displacement data show that shear-speed can be quantitatively identified with good accuracy, and that shear-speed images show good contrast. The results also suggest that attenuation images are qualitatively useful for identifying boundaries in the image and in tissue characterization experiments

using large filter regions. Reconstructions perform better when both the motion and its second derivatives are large, providing a useful perspective for elastography estimation methods.

### ACKNOWLEDGMENTS

The authors gratefully acknowledge Alex Dresner and Jennifer L. Mahowald for help in obtaining the experimental data used in this paper. This work was supported in part by a graduate student fellowship from the National Science Foundation.

### APPENDIX

#### Explicit Inversion Formula

In this section we give the explicit formulas used to calculate  $M$  and  $\Lambda + M$ . This is an expansion of Eq. [5].

$$M = \frac{C_1 + C_2 + C_3}{D_1 - D_2}$$

$$\Lambda + M = \frac{C_4 + C_5 + C_6}{D_1 - D_2}$$

where

$$C_1 = \Phi_1[(|A_{31}|^2 + |A_{21}|^2)A_{12}^* - A_{11}^*(A_{22}^*A_{21} + A_{32}^*A_{31})]$$

$$C_2 = \Phi_2[(|A_{31}|^2 + |A_{11}|^2)A_{22}^* - A_{21}^*(A_{12}^*A_{11} + A_{32}^*A_{31})]$$

$$C_3 = \Phi_3[(|A_{11}|^2 + |A_{21}|^2)A_{32}^* - A_{31}^*(A_{12}^*A_{11} + A_{22}^*A_{21})]$$

$$C_4 = \Phi_1[(|A_{22}|^2 + |A_{32}|^2)A_{11}^* - A_{12}^*(A_{21}^*A_{22} + A_{31}^*A_{32})]$$

$$C_5 = \Phi_2[(|A_{12}|^2 + |A_{32}|^2)A_{21}^* - A_{22}^*(A_{11}^*A_{12} + A_{31}^*A_{32})]$$

$$C_6 = \Phi_3[(|A_{12}|^2 + |A_{22}|^2)A_{31}^* - A_{32}^*(A_{11}^*A_{12} + A_{21}^*A_{22})]$$

$$D_1 = |A_{11}|^2(|A_{22}|^2 + |A_{32}|^2) + |A_{21}|^2(|A_{12}|^2 + |A_{32}|^2) + |A_{31}|^2(|A_{12}|^2 + |A_{22}|^2)$$

$$D_2 = A_{11}^*A_{12}(A_{22}^*A_{21} + A_{32}^*A_{31}) + A_{21}^*A_{22}(A_{12}^*A_{11} + A_{32}^*A_{31}) + A_{31}^*A_{32}(A_{12}^*A_{11} + A_{22}^*A_{21})$$

$$= 2\text{Real}\{A_{11}^*A_{12}A_{22}^*A_{21} + A_{11}A_{12}^*A_{31}^*A_{32} + A_{21}^*A_{22}A_{31}A_{32}^*\}$$

and

$$\mathbf{A} = \begin{bmatrix} A_{11} & A_{12} \\ A_{21} & A_{22} \\ A_{31} & A_{32} \end{bmatrix} = \begin{bmatrix} \Phi_{i,11} & \Phi_{1,ii} \\ \Phi_{i,12} & \Phi_{2,ii} \\ \Phi_{i,13} & \Phi_{3,ii} \end{bmatrix}.$$

### REFERENCES

1. Muthupillai R, Rossman PJ, David J, Lomas DJ, Greenleaf JF, Riederer SJ, Ehman RL. Magnetic resonance imaging of transverse acoustic strain waves. *Magn Reson Med* 1996;36:266–274.

2. Gao L, Parker KJ, Lerner RM, Levinson SF. Imaging of the elastic properties of tissue. *Ultrasound Med Biol* 1996;22:959–977.
3. Sumi C, Suzuki A, Nakayama K. Estimation of shear modulus distribution in soft tissue from strain distribution. *IEEE Trans Biomed Engineering* 1995;42:193–202.
4. Sumi C, Nakayama K. A robust numerical solution to reconstruct a globally relative shear modulus distribution from strain measurements. *IEEE Trans Med Imaging* 1998;17:419–428.
5. Sarvazyan AP, Rudenko OV, Swanson SD, Fowlkes JB, Emelianov SY. Shear wave elasticity imaging: a new ultrasonic technology of medical diagnosis. *Ultrasound Med Biol* 1998;24:1419–1435.
6. Fatemi M, Greenleaf JF. Ultrasound-stimulated vibro-acoustic spectrography. *Science* 1998;280:82–85.
7. Catheline S, Wu F, Fink M. A solution to diffraction biases in sonoelasticity: the acoustic impulse technique. *J Acous Soc Am* 1999;105:2941–2950.
8. Muthupillai R, Lomas DJ, Rossman PJ, Greenleaf JF, Manduca A, Ehman RL. Magnetic resonance elastography by direct visualization of propagating acoustic strain waves. *Science* 1995;269:1854–1857.
9. Chenevert TL, Skovoroda AR, O'Donnell M, Emelianov SY. Elasticity reconstructive imaging via stimulated echo MRI. *Magn Reson Med* 1998;39:482–490.
10. Romano AJ, Shirron JJ, Bucaro JA. On the noninvasive determination of material parameters from a knowledge of elastic displacements: Theory and simulation. *IEEE Trans Ultrason Ferroelec Frequency Cont* 1998;45:751–759.
11. Van Houten EEW, Paulsen KD, Miga MI, Kennedy FE, Weaver JB. An overlapping subzone technique for MR-based elastic property reconstruction. *Magn Reson Med* 1999;42:779–786.
12. Dutt V, Kinnick RR, Muthupillai R, Oliphant TE, Ehman RL, Greenleaf JF. Acoustic shear-wave imaging using echo ultrasound compared to magnetic resonance elastography. *Ultrasound in Medicine & Biology* 2000;26(3):397–403.
13. Marsden JE, Hughes TJR. *Mathematical foundations of elasticity*. Englewood Cliffs, NJ: Prentice-Hall Inc.; 1983. p 1–10.
14. Fung Y-C. *Biomechanics: mechanical properties of living tissues*, 2nd ed. Springer-Verlag; 1993.
15. Oliphant TE, Ehman RL, Greenleaf JF. Magnetic resonance elastography revisited: reinterpreting phase-difference data as the output of a linear filter. In: *Proceedings of the 8th Annual Meeting of ISMRM*, Denver, 2000. p 539.
16. Sinkus R, Lorenzen J, Schrader D, Lorenzen M, Dargatz M, Holz D. High-resolution tensor MR elastography for breast tumour detection. *Phys Med Biol* 2000;45:1649–1664.
17. Auld BA. *Acoustic fields and waves in solids*, Vol. II, 2nd ed. Krieger Publishing Company; 1990. p 21–38.
18. Muthupillai R, Dutt V, Rossman PJ, Hulshizer TC, Manduca A, Ehman RL. Three dimensional magnetic resonance elastography with multi-axis motion encoding. In: *Proceedings of the 5th Annual Meeting of ISMRM*, Vancouver, Canada, 1997. p 460.
19. Dumoulin CL, Souza SP, Darrow RD, Pelc NJ, Adams WJ, Ash SA. Simultaneous acquisition of phase-contrast angiograms and stationary-tissue. *J Magn Reson Imaging* 1991;1:399–404.
20. Savitsky A, Golay MJE. *Anal Chem* 1964;36:1627–1639.
21. Knutsson H, Westin C-F, Granlund G. Local multiscale frequency and bandwidth estimation. In: *Proceedings of ICIP-94*, vol 1, Los Alamitos, CA, 1994. IEEE Computer Society. p 36–40.